

# ISO SWS OBSERVATIONS OF H II REGIONS IN NGC 6822 AND I ZW 36: SULFUR ABUNDANCES AND TEMPERATURE FLUCTUATIONS<sup>1</sup>

Joshua G. Nollenberg, Evan. D. Skillman

*Astronomy Department, School of Physics and Astronomy, University of Minnesota, 116  
Church St. S.E., Minneapolis, MN 55455*

[manawa@astro.umn.edu](mailto:manawa@astro.umn.edu), [skillman@astro.umn.edu](mailto:skillman@astro.umn.edu)

Donald R. Garnett

*Steward Observatory, University of Arizona, 933 N. Cherry Ave., Tucson, AZ 85721*

[dgarnett@as.arizona.edu](mailto:dgarnett@as.arizona.edu)

and

Harriet L. Dinerstein

*Department of Astronomy, University of Texas at Austin, Austin, TX 78712*

[harriet@astro.as.utexas.edu](mailto:harriet@astro.as.utexas.edu)

## ABSTRACT

We report *ISO* SWS infrared spectroscopy of the H II region Hubble V in NGC 6822 and the blue compact dwarf galaxy I Zw 36. Observations of Br $\alpha$ , [S III] at 18.7 and 33.5 $\mu$ m, and [S IV] at 10.5 $\mu$ m are used to determine ionic sulfur abundances in these H II regions. There is relatively good agreement between our observations and predictions of S $^{+3}$  abundances based on photoionization calculations, although there is an offset in the sense that the models overpredict the S $^{+3}$  abundances. We emphasize a need for more observations of this type in order to place nebular sulfur abundance determinations on firmer ground. The S/O ratios derived using the *ISO* observations in combination with optical data

---

<sup>1</sup>Based on observations with ISO, an ESA project with instruments funded by ESA member states (especially the PI countries: France, Germany, the Netherlands, and the United Kingdom) and with the participation of ISAS and NASA.

are consistent with values of S/O, derived from optical measurements of other metal-poor galaxies.

We present a new formalism for the simultaneous determination of the temperature, temperature fluctuations, and abundances in a nebula, given a mix of optical and infrared observed line ratios. The uncertainties in our ISO measurements and the lack of observations of [S III]  $\lambda 9532$  or  $\lambda 9069$  do not allow an accurate determination of the amplitude of temperature fluctuations for Hubble V and I Zw 36. Finally, using synthetic data, we illustrate the diagnostic power and limitations of our new method.

*Subject headings:* infrared: spectra - nebulae: abundances - nebulae: H II regions - spectra: diagnostics

## 1. Introduction

Because of their low metallicities (Pagel & Edmunds 1981; Skillman, Kennicutt, & Hodge 1989; Izotov & Thuan 1999), dwarf irregular and blue compact galaxies can provide valuable information for a wide variety of astrophysical problems. By comparing the low metal abundances found in dwarf galaxies to abundances found in luminous spirals, one can infer variations in star formation histories and chemical evolution. It is possible to use measurements of abundances in H II regions in dwarf irregular galaxies to establish limits on yields from stellar and big bang nucleosynthesis (Pagel et al. 1992). It is also possible to characterize the ionizing radiation from OB stars from measurements of emission lines in H II region spectra without resolving individual stellar spectra (Vilchez & Pagel 1988).

Heavy elements such as C, N, O, Ne, S, and Ar are typically observed in H II regions. In order for accurate abundances to be determined, it is necessary to observe all of the ionization stages present in an H II region, or to have a reliable method for inferring the contribution of unobserved ions. Of the aforementioned elements, oxygen is the only one for which all important ionization stages can be easily observed at optical wavelengths. In the case of sulfur, the primary optical lines are [S II]  $\lambda\lambda 6717, 6731$  and [S III]  $\lambda 6312$ . However, the [S III]  $\lambda 6312$  line is an extremely weak and temperature sensitive line, making it difficult to measure in many H II regions. Because a significant fraction of the sulfur in an H II region is in the ionization state S<sup>+2</sup> (Garnett 1989), accurate determination of S/H = N(S)/N(H) can be difficult based on optical measurements alone. The [S III]  $\lambda\lambda 9069, 9532$  lines in the near-infrared, which are intrinsically much stronger, often require a correction for atmospheric water absorption. In high-ionization nebulae S<sup>+3</sup>, which emits only in the  $10.5\mu\text{m}$  line, can also become an important constituent.

Furthermore, the depth of particular ionization zones, temperature fluctuations ( $t^2$ ), and other variations throughout a nebula can cause optical/UV forbidden line diagnostics to yield temperatures that are larger than ion-weighted average values in photoionization models, and they can weight emissivities toward values found in higher temperature regions of the nebulae (Peimbert 1967; Garnett 1992; Mathis, Torres-Peimbert, & Peimbert 1998; Esteban et al. 1999). These potential problems motivate the use of temperature insensitive mid- and far-infrared forbidden fine structure transitions in order to include optically unobserved ions, accurately determine nebular abundances, and to determine the amplitude and scale of temperature fluctuations inside H II regions (e.g., Dinerstein, Lester & Werner 1985). The infrared portion of the spectrum contains strong emission lines such as [S III]  $18.7\mu\text{m}$  and [S IV]  $10.5\mu\text{m}$ . For faint extragalactic H II regions, the high background flux from earth’s atmosphere precludes ground-based observations of many middle- and far-infrared emission lines at the present time. However, the low background and high sensitivity of the ISO observatory allowed observations to be made of many faint extragalactic sources.

In this paper, we present mid-infrared *ISO* spectra of the [S III]  $18.7\mu\text{m}$  and  $33.5\mu\text{m}$  lines, plus the [S IV]  $10.5\mu\text{m}$  line, from the H II region Hubble V in NGC 6822 (hereafter referred to as Hubble V), and the blue compact galaxy I Zw 36 (MRK 209; UGCA 281). Our goal is to compare our infrared observations with published optical observations in order to test whether the theoretically predicted ionization correction factors are correct and to determine whether temperature fluctuations are large enough to be detectable in this manner.

## 2. Observations

### 2.1. ISO Observations

Observations of Hubble V and I Zw 36 were obtained using the Short Wavelength Spectrometer (SWS) (de Graauw et al. 1996) on the 60 cm Infrared Space Observatory (*ISO*) (Kessler et al. 1996). Details of these observations are given in Table 1. The Astronomical Observation Template (AOT) AOT02 was used to measure individual lines in a narrow bandpass with a width of  $\Delta\lambda/\lambda \approx 0.01$  (Leech 1997). Although line profiles were oversampled with the SWS, the instrumental profile FWHM of about  $150\text{ km s}^{-1}$  is much larger than the intrinsic widths of emission lines from H II regions. The Br $\alpha$  and [S IV]  $10.5\mu\text{m}$  lines were observed through a  $14''\times20''$  aperture, while the [S III]  $18.7\mu\text{m}$  line was measured through a  $14''\times27''$  aperture. We also obtained measurements of [S III]  $33.5\mu\text{m}$  through a  $20''\times33''$  aperture, but these observations had poor signal/noise and were not used.

Standard *ISO* reduction techniques were employed to reduce the data, using the latest photometric calibrations and procedures (SWS ia3) available at the time of the data reduction (Leech 1997). The following paragraphs illustrate some of the difficulties and challenges involved in the reduction of the *ISO* data.

Each *ISO* observation begins with a photometric check, which is a detector scan of an internal calibration source. This is followed by a series of dark current scans and integrations on the source. Memory effects, fringing, glitches and floating dark current levels seriously degraded the quality of the data that were obtained with the SWS. Each of these problems were evident upon preliminary review of the data. Therefore, it was necessary to work with staff scientists and programmers at IPAC to correct the data by using the Interactive Analysis packages that have been developed.

The memory effects were primarily due to the measurement of the internal calibration sources at the beginning of each observation. The intensity of the calibrators was high enough to cause the detectors to produce artificially high readings while performing subsequent dark scans and observations. This latent signal that persisted after illumination by bright sources was primarily evident in Detector Bands 1 and 2. During the Interactive Analysis, memory effects were corrected first, using the *antimem* IDL routine that was designed specifically for this purpose.

The second effect that we corrected for was the variation in dark current readings. At regular intervals while observing an object, the detector would perform a dark current scan. Because of time-dependent and nonlinear detector response effects (e.g., memory effects, changing noise levels, and “glitches”), dark current subtractions by the automated processing pipeline were often inaccurate, especially for very faint continuum sources. The dark scans were corrected by hand using the *dark\_inter* algorithm. First, each individual dark scan was sigma clipped about the median of the scan using a threshold of  $3\sigma$ . In severe cases, entire dark scans were thrown out (especially dark scans that suffered from memory effects because they immediately followed a photometric check). Individual scans were also deglitched, as will be discussed later. While making the dark current corrections, it was necessary to determine whether the dark current level, which appeared to jump at random time intervals, actually correlated with the subsequent object scan. In cases where there was bimodality, in which the voltage readout fluctuated between two levels from one readout point to the next on very short timescales, only those points which corresponded to the dark level of the object scans were used. Use of these corrected dark levels resulted in a marked improvement of the quality of dark subtraction.

Variations in sensitivity were also a problem in the *ISO* detectors (Leech 1997). Generally, these variations were time-dependent and nonlinear. Variations from orbit to orbit

were often caused by passage through the Van Allen Radiation Belts, cosmic ray strikes and observation of bright objects. However, small variations could be corrected using the *spd-rl* routine in the Interactive Analysis package.

Once the above operations using the Interactive Analysis package were completed, the data were processed further using the *ISO* Spectral Analysis Package (ISAP). First, glitches flagged by the initial pipeline processing were removed using the algorithm provided in ISAP. Generally, about 30% of the total number of data points were rejected including some entire scans.

Another concern is whether any flux was inadvertently lost or gained due to *ISO*’s nominal  $\approx 1''$  pointing error. The SWS apertures cover an area larger than I Zw 36, which has an angular extent of roughly  $10'' \times 11''$  as well as Hubble V, with a FWHM of  $5.5''$  (Collier, Hodge, & Kennicutt 1995). A thorough review of the current readouts from each observation showed no systematic variation with time, only occasional spikes due to cosmic ray hits and noise. Variations in the average current level would have indicated that the objects were falling in and out of the aperture during the scans. This implies that pointing error or jitter did not cause the objects to fall out of the aperture. The observed *ISO* line fluxes for I Zw 36 and NGC 6822 are given in Table 2, and plots of the spectra can be found in Figure 1.

Estimates of the magnitudes of flux calibration uncertainties were given in Leech (1997) for several of these problems. Uncertainties due to the memory effects were reported to be on the order of 6 – 15% in Band 2 ( $\text{Br}\alpha$ ) and 8 – 30% in Band 4 ([S III]  $18.7\mu\text{m}$  and [S IV]  $10.5\mu\text{m}$ ). Therefore there is a potential uncertainty of up to nearly 50% in the relative flux calibrations between bands. Furthermore, the Spectral Energy Distributions of standard objects used in flux calibrations are known only to between 4 – 10%. These systematic uncertainties are not included in the line flux errors cited in Table 2.

## 2.2. Supporting Observations from the Literature

There exist several sources of published optical data for Hubble V (Lequeux et al. 1979; Pagel, Edmunds & Smith 1980; Skillman, Terlevich, & Melnick 1989; Miller 1996) and I Zw 36 (Viallefond & Thuan 1983; Izotov, Thuan & Lipovetsky 1997) which allow a comparison of the abundances derived from optical and infrared [S III] transitions. Observed values of line ratios relevant to this paper are given in Table 3. A comparison of the abundances derived from these sources with the abundances derived from our *ISO* observations can be found in §3.3. Of the Hubble V observations, only those of Lequeux et al. (1979) include a

measurement of the [S III]  $\lambda 6312$  line through a large aperture. We therefore adopt these optical observations for comparison with our infrared measurements. Note that the reddening corrections for the infrared emission line ratios used in this paper are negligible.

### 3. Data Analysis

#### 3.1. Electron Temperatures and Densities

Prior to determining the ionic abundances from the data, electron temperatures were computed using a combination of existing published optical diagnostic data and updated atomic data from Pradhan & Peng (1995). In the case of Hubble V, four sources had [O III] data: Pagel & Edmunds (1981), Lequeux et al. (1979), Skillman, Terlevich, & Melnick (1989), and Miller (1996). From these sources, the diagnostic ratio

$$R(O\ III) = \frac{I(\lambda 4959) + I(\lambda 5007)}{I(\lambda 4363)} \quad (1)$$

was determined. These line ratios and the derived electron temperatures are given in Table 4. Adopting the Lequeux et al. (1979) data, the electron temperature for Hubble V was determined to be  $T_e = 11,200 \pm 1,100$  K. This value is consistent, within stated errors, with the other observations and was adopted for the calculation of emissivities in the abundance calculations. Viallefond & Thuan (1983) and Izotov, Thuan & Lipovetsky (1997) have reported optical spectroscopy for I Zw 36. Using the emission line fluxes from Viallefond & Thuan (1983), we obtain an electron temperature of  $14,600 \pm 500$  K, a result which corresponds closely to that given by Viallefond & Thuan (1983):  $T_e = 14,500 \pm 1,300$  K. However, using fluxes from Izotov, Thuan & Lipovetsky (1997) with smaller relative observational errors, we obtained a value of  $T_e = 16,180 \pm 70$  K, which we adopt.

Photoionization models indicate that the electron temperature is not uniform across an H II region, but can be different for low-ionization and high-ionization zones, depending on metallicity (Garnett 1992). We use the formulation given in Garnett (1992) to estimate electron temperatures for the O<sup>+</sup> and S<sup>+2</sup> zones, based on the derived [O III] temperature. We derive  $T(O^+) = 10,800 \pm 1,200$  K for Hubble V and  $T(O^+) = 14,330 \pm 50$  K for I Zw 36, while  $T(S^{+2}) = 11,000 \pm 1,200$  K and  $15,130 \pm 50$  K for Hubble V and I Zw 36, respectively. Since the temperatures in the low ionization zones are not observed directly, but rather are derived from photoionization models, we assume a lower limit of 500 K on the uncertainty when deriving abundances.

Published spectroscopic results for these two regions give low electron densities,  $n_e < 200$  cm<sup>-3</sup> based on [S II] line ratios. These densities are too small to cause significant collisional

de-excitation of the [S III] and [S IV] lines. Because of the poor signal/noise in the  $33.5\mu\text{m}$  observations, these infrared [S III] line measurements do not provide meaningful constraints on  $n_e$ .

### 3.2. Abundance Calculations

Using the values of electron temperature derived in the previous section, we computed ionic abundances using a 5-level atom for  $\text{O}^+$ ,  $\text{O}^{+2}$ ,  $\text{S}^+$ , and  $\text{S}^{+2}$  from the published optical emission line data for Hubble V and I Zw 36. Collision strengths for [O II], [O III], and [S II] transitions were taken from the compilation of Pradhan & Peng (1995). Collision strengths for [S III] were taken from the 27-state R-matrix calculation of Tayal & Gupta (1999), while for [S IV] we took the results of the 24-state calculation of Tayal (2000). Our computed abundances are listed in Table 5. We note that the new values of the effective collision strengths for the [S III] infrared fine-structure transitions represent an increase of  $\approx 30\%$  over those of Galavís, Mendoza & Zeippen (1995).

$\text{S}^{+3}$  can represent a substantial fraction of the total sulfur abundance in many H II regions (e.g., Lester, Dinerstein, & Rank 1979; Pipher et al. 1984). Garnett (1989) (see also Garnett et al. 1997) showed that there is a sharp decrease in the observed ratio  $(\text{S}^+ + \text{S}^{+2})/\text{O}$  for  $\text{O}^+/\text{O} < 0.25$ , indicating an increasing contribution from  $\text{S}^{+3}$  in high ionization H II regions (where ionization is parameterized by  $\text{O}^+/\text{O}$ ). However, the contribution of  $\text{S}^{+3}$  often remains uncertain because [S IV] has no optical transitions; the only line in the ground configuration is at a wavelength of  $10.51\mu\text{m}$ . In most cases photoionization models are used to estimate the  $\text{S}^{+3}$  contribution. Dinerstein (1980) demonstrated that sulfur ionization correction factors based on coincidences in ionization potentials greatly overpredict the actual amount of  $\text{S}^{+3}$  in high-ionization planetary nebulae. However, the accuracy of ionization corrections based on photoionization models is largely untested for H II regions, since very few observations exist for [S III] and [S IV] in comparable beam sizes. Therefore, an important aspect of this study is the inclusion of [S IV] in the estimation of the total nebular sulfur abundance.

Here, we determine  $\text{S}^{+2}$  and  $\text{S}^{+3}$  abundances from our *ISO* observations of the infrared fine structure lines [S III]  $18.7\mu\text{m}$  and [S IV]  $10.5\mu\text{m}$ . We normalized the IR fine-structure lines to our  $\text{Br}\alpha$  measurements also made with the SWS. Because the extinction coefficients are low in the IR and even the optical extinction to these two targets are low, the reddening corrections are negligible. Given the nebular physical conditions derived in Section 3.1, we computed the  $\text{S}^{+2}$  and  $\text{S}^{+3}$  abundances listed in Table 5. We used only the  $18.7\mu\text{m}$  line to derive the  $\text{S}^{+2}$  abundance, because of the low signal/noise for our  $33.5\mu\text{m}$  measurements.

Theoretical models and observational studies have indicated that the S/O ratio remains constant with respect to the oxygen abundance, O/H, regardless of metallicity (Fran ois 1988; Torres-Peimbert, Peimbert, & Fierro 1989; Garnett 1989; Izotov & Thuan 1999). In Figure 2 we plot our newly-derived S/O values for Hubble V and I Zw 36, along with values for other objects obtained from the literature, vs. O/H. Figure 2 shows that both I Zw 36 and Hubble V have S/O values similar to those of other metal-poor H II regions. This result tends to support the validity of the abundance ratios derived from optical spectroscopy.

### 3.3. Photoionization Models

Current photoionization models are limited in accuracy because of uncertainties in input parameters such as stellar ionizing flux distributions. V lchez & Pagel (1988) proposed the use of the ratio

$$\eta = \frac{O^+/O^{+2}}{S^+/S^{+2}} \quad (2)$$

as an indicator of the “hardness” of the photoionizing radiation field inside a nebula, which can be used to infer the effective temperature ( $T_*$ ) of the ionizing cluster. Garnett (1989) showed that this is indeed an useful estimator of relative values of  $T_*$  in nebulae by constructing photoionization models using different stellar atmosphere flux distributions. However, it may not be possible to derive absolute values of  $T_*$  from  $\eta$ , and it begins to lose its sensitivity above  $T_{eff} \sim 45,000$ K, as shown by Skillman (1989). Values of  $\eta$  for each nebula were calculated using the O/H ratios as well as the  $(S^++S^{+2})/S$  values from Table 5 and are also listed there. Using Figure 6 of Garnett (1989) and Figure 1 of V lchez & Pagel (1988) we find that the  $\eta$  parameter for Hubble V is consistent with  $T_* \approx 45,000$ K (using Hummer & Mihalas 1970 LTE model atmospheres) while the  $\eta$  parameter for I Zw 36 is consistent with  $T_*$  greater than 50,000K. This is within the range of values of  $\eta$  for other giant extragalactic H II regions and consistent with excitation by a mixture of hot O and B type stars (cf. Garnett 1989). In the specific case of Hubble V, Bianchi et al. (2001) reproduce the H-R diagram for the most luminous stars in OB 8, the stellar association powering Hubble V, and it appears that 45,000 K is a conservative upper limit to the effective temperatures of the most massive stars in this association.

Early studies of sulfur abundances in H II regions noted that neglecting the contribution of  $S^{+3}$  would result in an underestimate of the total sulfur abundance (e.g., Stasi ska 1978; French 1981). The photoionization models of Garnett (1989) showed a clear relationship between the  $S^{+3}$  ionization correction and  $O^+/O$  which is relatively insensitive to stellar effective temperature or abundance. In Figure 3, we show  $O^+/O$  vs.  $\log (S^++S^{+2})/S$  for the two observed nebulae and compare them to the models of Stasi ska (1990) for two different

sequences in stellar effective temperature. The model sequences represent abundances of 0.1 times solar, similar to the metallicities of our two objects. The values for Hubble V and I Zw 36 plotted in Figure 3 fall at slightly higher values of  $(S^+ + S^{+2})/S$  or lower values of  $O^+/O$  than the models. This may indicate that the  $S^{+3}$  fraction is overestimated in the models, perhaps due to line blanketing not accounted for in the stellar atmosphere fluxes. However, we caution against over-interpretation of this offset given the mismatch between the apertures for the optical and IR observations and the fact that the points in Figure 3 are less than  $2\sigma$  away from the model curves. We emphasize that more observations of  $S^+$ ,  $S^{+2}$ , and  $S^{+3}$  for the same object (preferably with matched apertures) will provide a valuable consistency check on the ICF for  $S^{+3}$ . Corrections for the unobserved  $S^{+3}$  abundance are now usually carried out based on photoionization modeling (e.g., the Thuan, Izotov, & Lipovetsky 1995 fit to the models of Stasińska 1990). It is still desirable to have observational tests of these fits spanning a large range in excitation. With the advent of more sensitive IR instruments, it may eventually be possible to characterize the effective temperatures of the ionizing stars, and to determine the best nebular models to describe a given H II region.

## 4. DIAGNOSTICS AND TEMPERATURE FLUCTUATIONS

### 4.1. Standard Analysis of Temperature Fluctuations

Because optical collisionally excited line emission is weighted toward high temperature regions, abundance measurements based on optical data may not provide the true ionic abundance of a species in the H II region (Peimbert 1967; Garnett 1992; Mathis 1995; Steigman, Viegas, & Gruenwald 1997). This effect would be most extreme in a case where there is a very localized zone of high temperature embedded in a more extended, lower temperature nebula. In this case, a calculation of the  $S^{+2}$  abundance from  $[S\text{ III}]\lambda 6312$  would yield a  $S^{+2}$  abundance lower than the true value. However, this problem can be rectified by observing lines with much smaller excitation energies, i.e. infrared fine structure transitions. Because of their lower excitation energy, the volume emissivities for such transitions are insensitive to electron temperature, and as a result, emission line ratios can be converted to ionic abundances with a smaller dependence on temperature variations within the ionized gas (e.g., Dinerstein 1986). The measurement of larger abundances of an ion from infrared line observations than from optical lines would thus be an indication that there may be temperature fluctuations inside a nebula. Dinerstein, Lester, & Werner (1985) used such an approach to estimate the magnitude of temperature fluctuations in several planetary nebulae using a combination of infrared and optical  $[\text{O III}]$  lines. Comparison of the  $S^{+2}$  abundances in Table 5 show evidence of the effect of temperature fluctuations in I Zw 36 and Hubble V,

although this is only significant at the  $1-2\sigma$  level.

Peimbert (1967) first determined the effects of temperature fluctuations on the calculation of nebular temperatures themselves through a density-weighted ensemble average of the temperature,

$$T_o(N_i, N_e) = \frac{\int T(r) N_i(r) N_e(r) d\Omega dl}{\int N_i(r) N_e(r) d\Omega dl}, \quad (3)$$

derived from an emission line. This average temperature, used in conjunction with an emission temperature, defined by:

$$\frac{I_{X+p, \lambda_{nm}}}{I_{X+p, \lambda_{n1m1}}} = \exp \left[ -\frac{\Delta E - \Delta E^*}{kT} \right], \quad (4)$$

where  $\Delta E$  and  $\Delta E^*$  are the excitation energies of the two lines, can be used to define the root mean square temperature fluctuation,

$$t^2 = \langle \left[ \frac{T(r) - T_o}{T_o} \right]^2 \rangle. \quad (5)$$

Then, assuming small fluctuations, one can perform a Taylor expansion, and relate the emission temperature to the average temperature by:

$$T \approx T_o \left[ 1 + \left( \frac{\Delta E + \Delta E^*}{kT_o} - 3 \right) \frac{t^2}{2} \right], \quad (6)$$

where  $\Delta E \neq \Delta E^*$  and  $t^2 \ll 1$ .

An alternative formalism was created by Mathis (1995) in which a fraction,  $C$ , of the gas is assumed to be at one temperature,  $T_1$ , while the rest of the gas is assumed to be at a second temperature,  $T_2$ . From this, one can estimate the degree to which differing amounts of plasma at each temperature can affect the derived abundances through the optical depth:  $d\tau/dT = C\delta(T - T_1) + (1 - C)\delta(T - T_2)$ , where  $d\tau = n_e n(X) ds$ .

## 4.2. A New Approach to Characterizing Temperature Fluctuations

We have developed a different approach that can be used to characterize the average temperature and the root-mean-square temperature fluctuations in a region. This method can be used with an arbitrary temperature distribution.

Assume the gas in a nebula follows a Gaussian temperature distribution, with mean temperature,  $T_o$ , and a dispersion  $\sigma_T$ . Let us also assume that the emission lines that we

are observing have emission coefficients, at constant density, that can be characterized over a temperature range of a few times  $\sigma_T$  by a quadratic fit,

$$\epsilon_{X_i, \lambda_i}(T) = a_{X_i, \lambda_i} T^2 + b_{X_i, \lambda_i} T + c_{X_i, \lambda_i}, \quad (7)$$

where  $a_{X_i, \lambda_i}$ ,  $b_{X_i, \lambda_i}$ , and  $c_{X_i, \lambda_i}$  are the coefficients of the quadratic fit of the emission coefficient. This is justified, because emission coefficients can usually be accurately approximated by quadratic polynomials over temperature ranges of several thousand degrees.

Then, the ratio of two emission line intensities ( $R$ ), which can be generally written as:

$$R = \frac{I_{X_1, \lambda_1}}{I_{X_2, \lambda_2}} = \frac{N_{X_1} N_e \epsilon_{X_1, \lambda_1}(T)}{N_{X_2} N_e \epsilon_{X_2, \lambda_2}(T)} \quad (8)$$

can be convolved with the normalized Gaussian temperature distribution so that we have:

$$\frac{I_{X_1, \lambda_1}}{I_{X_2, \lambda_2}} = \frac{N_{X_1} \int \epsilon_{X_1, \lambda_1}(T) p(T) dT}{N_{X_2} \int \epsilon_{X_2, \lambda_2}(T) p(T) dT}, \quad (9)$$

where

$$p(T) = \frac{1}{\sigma_T \sqrt{2\pi}} \exp \left[ \frac{(T - T_o)^2}{2\sigma_T^2} \right]. \quad (10)$$

Upon integration from  $T = -\infty$  to  $T = \infty$ , the relation becomes

$$\frac{I_{X_1, \lambda_1}}{I_{X_2, \lambda_2}} = \frac{N_{X_1}}{N_{X_2}} \frac{a_{\lambda_1} (\sigma_T^2 + T_o^2) + b_{\lambda_1} T_o + c_{\lambda_1}}{a_{\lambda_2} (\sigma_T^2 + T_o^2) + b_{\lambda_2} T_o + c_{\lambda_2}}, \quad (11)$$

which holds to a good degree of accuracy due to the square-exponential behavior of the kernel in the integrand. However, one should be aware that in this approximation, the Gaussian kernel,  $p(T)$ , has some mean temperature,  $T_o$ , and width,  $\sigma_T$ . If  $T_o \gg \sigma_T$ , then there are no problems, but if  $T_o \sim \sigma_T$ , then a significant portion of the kernel may correspond to temperatures  $T < 0K$ , which is clearly non-physical and the approximation breaks down. When  $T_o \geq 3\sigma_T$ , then less than 3% of the kernel will correspond to negative temperatures, and the approximation will hold.

Let the line ratio divided by the abundance be given by

$$\gamma_{12} = \frac{I_{X_1, \lambda_1}}{I_{X_2, \lambda_2}} \cdot \frac{N_{X_2}}{N_{X_1}}, \quad (12)$$

then it is possible to solve for the temperature fluctuations,  $\sigma_T^2$ , using the equation

$$\sigma_T^2 = \frac{(a_{\lambda 1} - \gamma_{12} a_{\lambda 2}) T_o^2 + (b_{\lambda 1} - \gamma_{12} b_{\lambda 2}) T_o + (c_{\lambda 1} - \gamma_{12} c_{\lambda 2})}{-(a_{\lambda 1} - \gamma_{12} a_{\lambda 2})}. \quad (13)$$

We will refer to Equation (13) as the “diagnostic equation.” Equation (13) yields a locus of points in  $T_o$ ,  $\sigma_T^2$  space: a curve for a single, fixed value for the observed line ratio,  $R$ , and, for different values of  $T_o$ , different Gaussian temperature distributions of variance  $\sigma_T^2(T_o)$  centered on  $T_o$ . So by using additional line ratios, one establishes a diagnostic in which it is possible to solve explicitly for the ionic temperature and the temperature fluctuations in the gas (as done for [O III] by Dinerstein, Lester, & Werner 1985). Furthermore, provided three or more collisionally excited lines relative to an H recombination line are available for a given ionic species, the abundance of that species can also be solved for simultaneously. The calculated temperature variance,  $\sigma_T^2$ , is related to the traditional  $t^2$  by definition:

$$\sigma_T^2 = T_o^2 t^2, \quad (14)$$

which holds even if the true distribution of the gas temperature is not Gaussian.

If a case arises in which a Gaussian distribution is not appropriate, this method is adaptable so that other (normalized) kernels can be applied as well. For example, assuming a normalized rectangle function (a top-hat) temperature distribution, with half-width  $\delta_T$ , given by:

$$p(T) = \begin{cases} \frac{1}{2\delta_T} & : T_L < T < T_U \\ 0 & : T \leq T_L, T \geq T_U. \end{cases}$$

Then one obtains an equation identical to (11), but of the form

$$\frac{I_{X_1, \lambda_1}}{I_{X_2, \lambda_2}} = \frac{N_{X_1}}{N_{X_2}} \frac{a_{\lambda_1} \left( \frac{1}{3} \delta_T^2 + T_o^2 \right) + b_{\lambda_1} T_o + c_{\lambda_1}}{a_{\lambda_2} \left( \frac{1}{3} \delta_T^2 + T_o^2 \right) + b_{\lambda_2} T_o + c_{\lambda_2}}. \quad (15)$$

keeping in mind that  $\delta_T^2$  can be related to  $\sigma_T^2$  by:

$$\sigma_T^2 = \frac{1}{3} \cdot \delta_T^2. \quad (16)$$

Other distribution functions that also could be used include the Lorentzian distribution or the Triangle distribution with a base width of  $b_T$ , given by

$$p(T) = \begin{cases} \frac{T - T_o + b_T}{b_T^2} & : T_o - b_T < T < T_o + b_T \\ \frac{-T + T_o + b_T}{b_T^2} & : T_o < T < T_o + b_T \\ 0 & : \text{otherwise.} \end{cases}$$

The Triangle distribution and a truncated Lorentzian distribution which has limits placed on the width of the wings at its base also yield equation (11). For the Triangle distribution,  $\sigma_T^2 = 1/6 \times \delta_T^2$ , while the truncated Lorentzian possesses a more complicated relationship between its width, base limits, and  $\sigma_T^2$ .

### 4.3. Behavior of the Diagnostic and Choice of Line Ratios

Initially, we tested the diagnostic by checking whether it would be able to determine the physical properties of a model of a gas cloud with an average temperature  $T_0 = 12,000$  K, temperature fluctuations  $\sigma_T = 2,000$  K, and an abundance approximately equal to that of Hubble V. We used emission coefficients given by the STSDAS *nebular.ionic* routine (Shaw & Dufour 1995), each of which was fitted using a second-order polynomial. Coefficients for these fits are listed in Table 6. Then the square root of equation (14) was plotted using various line ratios involving [S III] and [O III] forbidden lines and H recombination lines, assuming the physical conditions given above, by varying  $T_o$  in order to determine  $T_o$  and  $\sigma_T$  simultaneously. Figure 4 shows these diagnostic lines for the case of the nebula described above. The top panel shows diagnostics from combinations of [S III] and H recombination lines while the bottom panel shows diagnostics from combinations of [O III] lines. Diagnostics involving different combinations of emission lines have different sensitivities to temperature and temperature fluctuations. In order to simultaneously determine the temperature and the temperature fluctuations one would ideally use two combinations of emission lines that yield diagnostics that intersect at nearly right angles. For example, this is roughly the case in the top panel of Figure 4 between the [S III]  $\lambda 6312/18.7\mu m$  and the  $\lambda 9532/18.7\mu m$  diagnostics.

The models on which Figure 4 is based show an additional feature of the diagnostic. The diagnostics involving lines originating solely from one ion intersect at a point that is independent of ionic abundance. However, when using diagnostics that involve ratios of ionic to H recombination lines, this is no longer the case. Therefore, it is possible to simultaneously determine the ionic abundance as well as the temperature and temperature fluctuations, provided that strengths of enough emission lines are known so that the three unknowns can be calculated, and that the ions in question reside in regions of the same  $T_0$  and  $\sigma_T$ .

Because the diagnostics are comprised of ratios of emission lines with different temperature sensitivities (the  $\lambda 9532/18.7\mu m$  diagnostic, for example), the sensitivity of the diagnostic will vary with temperature. Graphically, the diagnostic lines appear to rotate as either the temperature or the temperature fluctuations are varied. Therefore it may be necessary to mix and match combinations of emission lines in order to have orthogonally-crossing diagnostic lines that provide the most stringent determination of the nebular parameters. A general rule of thumb for most nebular conditions would be to use combinations involving nebular (transitions between the middle and lowest terms in an ionic configuration, e.g. [S III]  $\lambda 9532$ ), auroral (transitions between the highest and middle terms, e.g. [S III]  $\lambda 6312$ ), and fine structure features.

#### 4.4. Application of the Diagnostic Technique

An optimal combination of emission lines consisting of the nebular, auroral, and fine-structure lines of an ionic species as well as hydrogen recombination lines will allow the simultaneous determination of the nebular temperature, temperature fluctuations, and the abundance of the species with respect to hydrogen (see Equation 13). Unfortunately, for most H II regions, published observations do not exist for all of these types of transitions (or, as in the present case, they have not been observed through matched apertures), so we are unable to use our diagnostic technique fully with the present data. However, in this section we will demonstrate the use of the diagnostic using two approaches. First, we will demonstrate the usefulness of the diagnostic using our *ISO* and ground-based measurements for Hubble V and I Zw 36. This exercise will not lead to accurate estimates of  $T$ ,  $\sigma_T$ , and abundances, because of the relatively large uncertainties in the line ratios and the fact that we did not have an optimal set of [S III] line ratios. However, it will serve as an illustration of the method on real data. Next, we will show the ability of the diagnostic to make rough predictions of the conditions inside a nebula using synthetic data.

##### 4.4.1. Illustration with real data

For Hubble V and I Zw 36 we have measurements of [S III]  $\lambda 6312$ ,  $18.7\mu\text{m}$ , and H recombination lines. Thus, we have essentially only two diagnostic line ratios, which is not sufficient to determine  $T_0$ ,  $\sigma_T^2$  and the  $\text{S}^{+2}$  abundance simultaneously. Another [S III] line, for example the nebular [S III] 9532 Å transition, is needed for a full solution.

Nevertheless, we can still provide an instructive example and set constraints on  $\sigma_T$  if we assume that the  $\text{S}^{+2}$  abundances that we calculated from our *ISO* [S III]  $18.7\mu\text{m}$  observations are correct. This abundance was based on the measurement of the electron temperature from the [O III] lines and an assumption of no temperature fluctuations. In principle, this assumption should be ok because the fine-structure lines have weak sensitivity to temperature fluctuations. How bad is this assumption? From equation (4) in Garnett (1992), which is just an update of Peimbert (1967) equation (15), we can get the ion-weighted mean electron temperature,  $T(\text{O}^{+2})$ , from the measured  $T(\text{O III})$  and an estimate of  $t^2$ . For  $T(\text{O III}) = 11,200$  K and a  $t^2$  value of 0.04,  $T(\text{O}^{+2}) = 10,000$  K. Since  $\text{S}^{+2}/\text{H}^+$  is roughly proportional to  $T^{-0.5}$  for the IR lines, for commonly claimed values of 0.03 to 0.04 for  $t^2$ , the uncertainty in the  $\text{S}^{+2}/\text{H}^+$  abundance is less than 10% (which is smaller than our quoted errors). Thus, this is probably not a bad assumption to adopt for an illustrative example.

The results are shown in Figure 5 for both Hubble V and I Zw 36, where it should

be noted that with the assumption of the  $S^{+2}/H$  abundance, we are left with only two undetermined variables:  $T$  and  $\sigma_T^2$ . This allows us to work in two dimensions and two diagnostics rather than three. We did, however, include a third diagnostic ( $\lambda 6312/18.7\mu m$ ) in Figure 5 to ensure that all of the diagnostic lines crossed at the same point and produced consistent results.

In Figure 5, the diagnostic curves are grouped by line ratio. The center line in each group represents the results of equation 13 for each observed line ratio; the parallel curves represent the spread caused by the  $\pm 1\sigma$  observational errors in the line ratios. The expected value of  $\sigma_T$  will lie at the centroid of the  $1\sigma$  error box. In section 3.2, we derived [S III] temperatures of  $11,000 \pm 1200K$  for Hubble V and  $15,130 \pm 50K$  for I Zw 36, based on the estimates from [O III] temperatures. Meanwhile, from the diagnostics in Figure 5 we obtain  $T[S III] \approx 12,000 \pm 1,000K$  for Hubble V, and  $15,500 \pm 1,000K$  for I Zw 36. Both of the values of  $T[S III]$  derived from Fig. 5 are in good agreement with those derived in Section 3.1.

The data presented in Figure 5 are consistent with a very large range in  $\sigma_T$  corresponding to values of  $t^2$  from 0 up to roughly 0.2, which is much larger than values usually considered. To provide better constraints on  $\sigma_T$  we would need to obtain higher quality observations of the infrared [S III] lines as well as include observations of [S III]  $\lambda\lambda 9069, 9532$ . In the next section we demonstrate the quality of data necessary for this goal.

#### 4.4.2. Illustration with synthetic data

The approach that was followed in Figure 5 is quite useful for the quick determination of the nebular conditions, however we have only used a rudimentary method for determining the errors associated with the original data. This problem is exacerbated by the fact that under some circumstances, the formal simultaneous solution of multiple diagnostics of the form given in Equation (14) may in fact yield  $\sigma_T^2 < 0$ . This could easily arise from observational uncertainties, but if the error propagation is carried out properly then one would expect the solution to be *consistent* with positive values for  $\sigma_T$ .

In order to develop a better understanding of the error analysis, we developed a Monte Carlo simulation to generate synthetic observations of line ratios whose values are specified along with their corresponding observational errors. The specified line ratios and errors are sent through the diagnostic so that each observation is plotted as a point on the  $\sigma_T^2$  vs.  $T$  plane. The intensity of points on the plane is the distribution that arises from a large number of observations, smeared by observational errors. We have plotted two examples of this in

Figure 6.

The top panel in Figure 6 shows the distribution of points that arises from [S III] line ratios corresponding to an isothermal nebula at  $T = 12,000K$ , with observational errors of 2% in optical and near-infrared lines ratios and 5% in line ratios with infrared lines. The peak of the distribution lies at the point that would be determined in the absence of observational errors. This plot also shows that roughly half of the realizations in the simulation yield  $\sigma_T^2 < 0$ . However, the contours corresponding to 1 and  $2\sigma$  errors in the determination of the nebular parameters show that the observations could correspond to small fluctuations. The  $1\sigma$  error corresponds to roughly  $t^2 \approx 0.04$ . Thus, it is possible to make significant constraints on temperature fluctuations using combinations of optical, near-infrared, and infrared [S III] lines. Similarly, the bottom panel of Figure 6 shows the distribution of realizations resulting from inputs corresponding to  $T = 12,000K$  and  $\sigma_T = 2,000K$  ( $\sigma_T^2 = 4 \cdot 10^6 K^2$ , which corresponds to  $t^2 = 0.028$ ), smeared by the same errors as above. It is now apparent that the diagnostic lines resulting from observations  $\pm 1\sigma$  errors do roughly correspond to the  $1\sigma$  bounds on the determinations of the nebular parameters.

Two things should be noted here. First, the low observational errors assumed in the calculations are difficult to achieve in practice, and matching apertures is critical. Long slit spectra of either spatially unresolved sources (e.g., extragalactic) or Galactic HII regions where the variations can be traced along the slit are probably best suited for this type of work. It is probably best to obtain ratios to H recombination lines in all cases (i.e., H $\alpha$  in the optical, P8, P9, and P10 in the near-infrared, and Br $\alpha$  in the infrared) to provide a normalization. Second, it is important to point out that for different temperature ranges, different ionic species will provide better constraints. For example, in the example presented in Figure 6, a combination of [O III] lines (with the same magnitude of relative errors) gives roughly a factor of two stronger constraint ( $t^2 \leq 0.02$ ) on the presence of temperature fluctuations.

## 5. SUMMARY AND CONCLUSIONS

We have reported new ISO observations of the mid-infrared fine structure [S III] and [S IV] lines. These lines are of great importance to the accurate determination of nebular total sulfur abundances. This is due to the strong dependence of higher excitation lines on temperature, along with the fact that there are no strong optical lines for either of these species. With our observations, we have shown that S $^{+3}$  can constitute a large fraction of the total sulfur abundance in extragalactic H II regions. This means that if one is to determine accurately the total sulfur abundance without model dependence as in equation (4), then one

must make infrared observations of the fine structure [S III] and [S IV] lines. Once infrared observations are made, it becomes possible to test not only useful techniques such as the determination of the radiation “hardness” (Vilchez & Pagel 1988) and the determinations of the total sulfur abundance as in equation (4) (Garnett 1989), but it becomes possible to test the accuracy of photoionization models. Our data suggest that ionization corrections for sulfur based on oxygen ion ratios and photoionization models are valid.

The presence of temperature fluctuations in nebulae can complicate the determination of nebular abundances. We have developed a new, generalized diagnostic capable of determining the amplitude of these fluctuations by assuming a Gaussian temperature distribution in these nebulae, although this method can be applied to any normalized distribution. The uncertainties in our ISO measurements and the lack of observations of [S III]  $\lambda 9532$  or  $\lambda 9069$  did not allow an accurate determination of the amplitude of temperature fluctuations for Hubble V and I Zw 36 using our method. A significant challenge is presented by combining large aperture infrared spectra with relatively small aperture optical spectra. Future long slit spectrographs available with SOFIA and SIRTF will allow us to overcome this challenge. As these more powerful instruments become available, observational uncertainties should decrease, allowing a more accurate determination of the size of the temperature fluctuations and other nebular parameters.

In the future, one can consider extensions to the present analysis. For example, the potential to calculate spatially unresolved density fluctuations in a similar mathematical framework remains relatively unexplored, although Rubin (1989) has considered the biasing of IR density indicators by density fluctuations. Like temperature fluctuations, density fluctuations can also affect nebular line ratios, and they may have significant effects on nebular physical parameters which must be constrained in order to develop better nebular models. To this end, application of this diagnostic to published data on a large number of H II regions may be useful in characterizing the variances found in H II regions.

We give special thanks to the Nancy Silbermann, Sergio Molinari, Sarah Unger and the rest of the IPAC staff for their assistance during and after our visit to IPAC during January, 1997. We also thank the referee, Manuel Peimbert, for a careful reading of the manuscript and several suggestions which significantly improved the paper. JN, EDS, and DRG acknowledge support from JPL contract 961500; DRG also acknowledges support from NASA LTSA grant NAG5-7714. HLD’s participation was supported by JPL contract 961543. EDS acknowledges support from NASA LTSA grant NAG5-9221 and the University of Minnesota.

## REFERENCES

- Bianchi, L., Scuderi, S., Massey, P., & Romaniello, M. 2001, AJ, 121, 2020
- Caplan, J., & Deharveng, L., 1986, A&A, 155, 297
- Collier, J., Hodge, P., & Kennicutt, R. 1995, PASP, 107, 361
- de Graauw, T, et al. 1996, A&A 315, L49
- Dinerstein, H. L. 1980, ApJ, 237, 486
- Dinerstein, H. L. 1986, PASP, 98, 979
- Dinerstein, H. L., Lester, D. F., & Werner, M. W. 1985, ApJ, 291, 561
- Esteban, C., Peimbert, M., Torres-Peimbert, S., García-Rojas, J., & Rodríguez, M., 1999, ApJS, 120, 113
- François, P. 1988, A&A, 195, 226
- French, H. B. 1981, ApJ, 246, 434
- Galavís, M. E., Mendoza, C. & Zeippen, C. J., 1995, A&ASS, 111, 347
- Garnett, D. R. 1989, ApJ, 345, 282
- Garnett, D. R. 1992, AJ, 103, 1330
- Garnett, D. R., Shields, G. A., Skillman, E. D., Sagan, S. P., & Dufour, R. J. 1997, ApJ, 489, 63
- Gruenwald, R. B. & Viegas, S. M. 1992, ApJS, 78, 153
- Hawley, S.A. 1978, ApJ, 224, 417
- Hummer, D.G. & Mihalas, D. 1970a, MNRAS, 147, 339
- Hummer, D.G. & Mihalas, D. 1970b, JILA Report No. 101
- Hummer, D.G. & Storey, P.J. 1987, MNRAS, 224, 801
- Izotov, Y. I. & Thuan, T. X. 1999, ApJ, 511, 639
- Izotov, Y. I., Thuan, T. X., Lipovetsky, V. A. 1997, ApJS, 108, 1
- Kessler et al., 1996, A&A, 315, L27

- Leech, K., 1997, *SWS Instrument Data Users Manual Issue 3.1*, SAI/95-221/Dc
- Lequeux, J., Peimbert, M., Rayo, J. F., Serrano, A., & Torres-Peimbert, S. 1979, A&A, 80, 155
- Lester, D. F., Dinerstein, H. L., & Rank, D. M. 1979, ApJ, 232, 139
- Mathis, J.S., RMxAASC, 3, 207
- Mathis, J. S., Torres-Peimbert, S., & Peimbert, M. 1998, ApJ, 495, 328
- Miller, B.W. AJ, 112, 991.
- Pagel, B. E. J. & Edmunds, M. G. 1981, ARA&A, 19, 77
- Pagel, B. E. J., Edmunds, M. G., Smith, G. 1980, MNRAS, 193, 219
- Pagel, B. E. J., Simonson, E. A., Terlevich, R. J., & Edmunds, M. G. 1992, MNRAS, 255, 325
- Peimbert, M. 1967, ApJ, 150, 825
- Pipher, J. L., Helfer, H. L., Herter, T., Briotta, D. A. Jr., Houck, J. R., Willner, S. P., & Jones, B. 1984, ApJ 285, 174
- Torres-Peimbert, S., Peimbert, M., & Fierro, J. 1989, ApJ, 345, 186
- Pradhan, A. K. & Peng, J. 1995, in The Analysis of Emission Lines, eds. R.E. Williams and M. Livio, Cambridge University Press, p. 8
- Rieke, G. H. & Lebofsky, M. J. 1985, ApJ, 288, 618
- Rubin, R. H., 1989, ApJS 69, 897
- Shaver, P.A., McGee, R.X., Newton, L.M., Danks,A.C., & Pottasch, S.R. 1983, MNRAS, 204, 53
- Shaw, R. A. & Dufour, R. J. 1995, PASP, 107, 896
- Skillman, E. D., Kennicutt, R. C., & Hodge, P. W. 1989, ApJ, 347, 875
- Skillman, E. D., & Klein, U. 1988, A&A, 199,61
- Skillman, E. D., Terlevich, R., & Melnick, J. 1989, MNRAS, 240, 563
- Stasińska, G. 1978, A&A, 66, 257

- Stasińska, G. 1990, A&AS, 83, 501
- Steigman, G., Viegas, S., Gruenwald, R. 1997, ApJ, 490, 187
- Tayal, S.S., 2000, ApJ, 530, 1091
- Tayal, S.S. & Gupta, G.P., 1999, ApJ, 526, 544
- Thuan, T.X., Izotov, Y. I., & Lipovetsky, V. A., 1995, ApJ, 445, 108
- Viallefond, F. & Thuan, T. X. 1983, ApJ, 269, 444
- Vílchez, J. M. & Pagel, B. E. J. 1988, MNRAS, 231, 257

Table 1. Journal of ISO SWS Observations

	Hubble V	I Zw 36
Observation date	17 Apr 1996	25 Apr 1996
Observer	DGARNETT	DGARNETT
TDT	15202208	16001210
Integration Time	588s	8040s

Table 2. Observed SWS Line Fluxes

Object	Wavelength ( $\mu m$ )	Species	Line Flux ( $W/cm^2$ )
Hubble V	4.05	Br $\alpha$	$(1.9 \pm 0.2) \times 10^{-20}$
	10.51	[S IV]	$(7.5 \pm 0.5) \times 10^{-20}$
	18.71	[S III]	$(6.7 \pm 0.7) \times 10^{-20}$
I Zw 36	4.05	Br $\alpha$	$(1.9 \pm 0.3) \times 10^{-21}$
	10.51	[S IV]	$(1.2 \pm 0.1) \times 10^{-20}$
	18.71	[S III]	$(4.9 \pm 1.0) \times 10^{-21}$

Table 3. Published Optical Line Strengths

$\lambda$ (Å)	Species	Hubble V			I Zw 36		
		LPRST79	PES80	STM89	M96	VT83	ITL97
3727	[O II]	1.4	1.5	$1.20 \pm 0.06$	$1.46 \pm 0.10$	0.7	$0.719 \pm 0.002$
4363	[O III]	0.052	0.047	$0.057 \pm 0.012$	$0.06 \pm 0.01$	0.12	$0.127 \pm 0.001$
4861	H $\beta$	1.00	1.00	1.00	1.00	1.00	1.00
4959	[O III]	1.8	1.6	$1.92 \pm 0.010$	$1.67 \pm 0.04$	1.98	$1.960 \pm 0.003$
5007	[O III]	5.4	5.0	$5.93 \pm 0.030$	$4.90 \pm 0.14$	6.52	$5.543 \pm 0.008$
6312	[S III]	0.014	...	...	...	0.017	$0.017 \pm 0.001$
6717	[S II]	0.063	0.09	$0.129 \pm 0.006^a$	...	0.042	$0.061 \pm 0.001$
6731	[S II]	0.045	0.06		...	0.031	$0.045 \pm 0.001$
$c(H\beta)$		0.8	1.05	0.7	$0.3 \pm 0.1$	$0.41 \pm 0.12$	0.00

<sup>a</sup>sum of blended  $\lambda 6716 + \lambda 6730$  (STM89 only)

Table 4. Electron Temperatures

Source	Object	R(O III)	$T_e$ (K)
LPRST79	Hubble V	137	11, 200
PES80	Hubble V	$142 \pm 31$	$11,000 \pm 900$
STM89	Hubble V	$138 \pm 47$	$11,500 \pm 1,000$
M96	Hubble V	$110 \pm 26$	$12,400 \pm 1,100$
VT83	I Zw 36	$70 \pm 12$	$14,600 \pm 1,300$
ITL97	I Zw 36	$59.08 \pm 0.47$	$16,180 \pm 65$

Table 5. Ionic and Total Abundances<sup>a</sup>

Abundance Ratio	Hubble V		I Zw 36	
	Optical	SWS	Optical	SWS
O <sup>+</sup> /H	3,800±900	...	710 ± 80	...
O <sup>+2</sup> /H	13,000±3,000	...	4,930 ± 40	...
O/H	16,800±3,100	...	5,640 ± 90	...
S <sup>+</sup> /H	20.1 ± 4.8	...	11.4 ± 0.6	...
S <sup>+2</sup> /H	250 ± 90	280 ± 50	95 ± 9	151 ± 30
S <sup>+3</sup> /H	...	65 ± 11	...	71 ± 13
S/H <sup>b</sup>	...	365 ± 51	...	233 ± 33
$\eta$	3.6±2.0	...	1.2±0.2	...

<sup>a</sup>All values are  $\times 10^{-8}$

<sup>b</sup>S/H = N(S<sup>+</sup>) (from optical data) + N(S<sup>+2</sup> + S<sup>+3</sup>) (from ISO data)

Table 6. Emission Coefficient Fit Parameters<sup>a</sup>

Species	$\lambda$ (Å)	$a_\lambda$	$b_\lambda$	$c_\lambda$
H I	$H\beta$	$6.072 \times 10^{-34}$	$-2.327 \times 10^{-29}$	$2.989 \times 10^{-25}$
H I	$Br\alpha$	$6.318 \times 10^{-35}$	$-2.427 \times 10^{-30}$	$2.811 \times 10^{-26}$
H I	$Br\gamma$	$2.058 \times 10^{-35}$	$-7.889 \times 10^{-31}$	$9.365 \times 10^{-27}$
[O III]	4363	$2.609 \times 10^{-30}$	$-3.828 \times 10^{-26}$	$1.446 \times 10^{-22}$
[O III]	4959	$-4.864 \times 10^{-31}$	$3.250 \times 10^{-25}$	$-1.958 \times 10^{-21}$
[O III]	5007	$-1.443 \times 10^{-30}$	$9.382 \times 10^{-25}$	$-5.651 \times 10^{-21}$
[O III]	$51.8\mu m$	$1.485 \times 10^{-30}$	$-5.523 \times 10^{-26}$	$1.335 \times 10^{-21}$
[O III]	$87.6\mu m$	$1.841 \times 10^{-30}$	$-7.676 \times 10^{-26}$	$1.931 \times 10^{-21}$
[S II]	4068	$7.652 \times 10^{-31}$	$9.599 \times 10^{-25}$	$-6.249 \times 10^{-21}$
[S II]	4076	$2.136 \times 10^{-31}$	$3.269 \times 10^{-25}$	$-2.122 \times 10^{-21}$
[S II]	6717	$-2.001 \times 10^{-28}$	$8.917 \times 10^{-24}$	$-3.734 \times 10^{-20}$
[S II]	6731	$-1.406 \times 10^{-28}$	$6.454 \times 10^{-24}$	$-2.729 \times 10^{-20}$
[S III]	6312	$3.884 \times 10^{-30}$	$5.208 \times 10^{-26}$	$-5.035 \times 10^{-22}$
[S III]	9069	$-2.622 \times 10^{-29}$	$1.079 \times 10^{-24}$	$-3.318 \times 10^{-21}$
[S III]	9532	$-1.448 \times 10^{-28}$	$5.960 \times 10^{-24}$	$-1.833 \times 10^{-20}$
[S III]	$18.7\mu m$	$3.929 \times 10^{-30}$	$-2.613 \times 10^{-25}$	$1.681 \times 10^{-20}$
[S III]	$33.5\mu m$	$6.407 \times 10^{-29}$	$-2.293 \times 10^{-24}$	$4.178 \times 10^{-20}$
[S IV]	$10.5\mu m$	$6.125 \times 10^{-29}$	$-3.409 \times 10^{-24}$	$8.859 \times 10^{-20}$

<sup>a</sup>applicable for  $n_e \leq 100 \text{ cm}^{-3}$

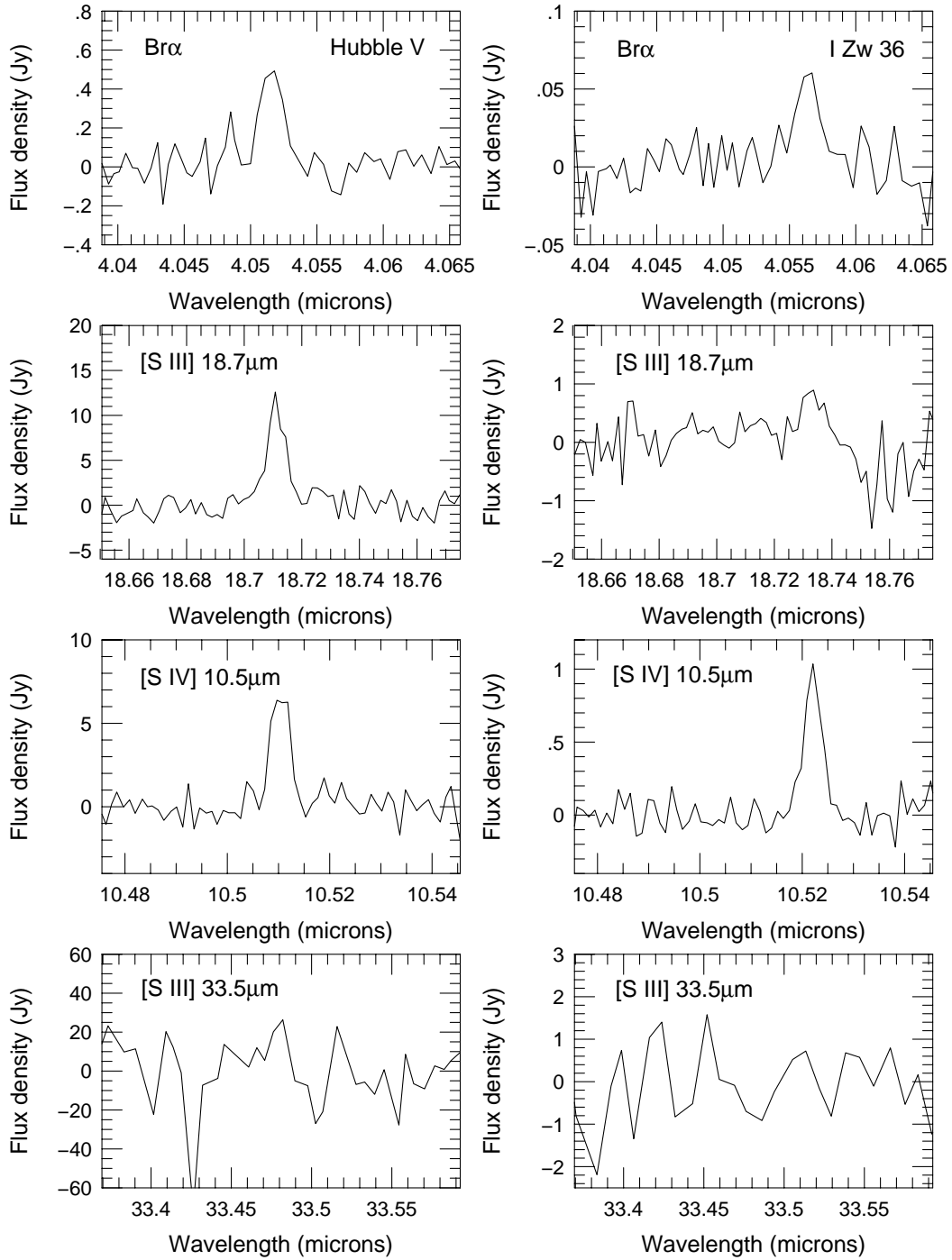


Fig. 1.— *ISO* Spectra of Br $\alpha$ , [S IV] 10.5 $\mu$ m, and [S III] 18.7 and 33.5 $\mu$ m spectral lines for Hubble V and I Zw 36.

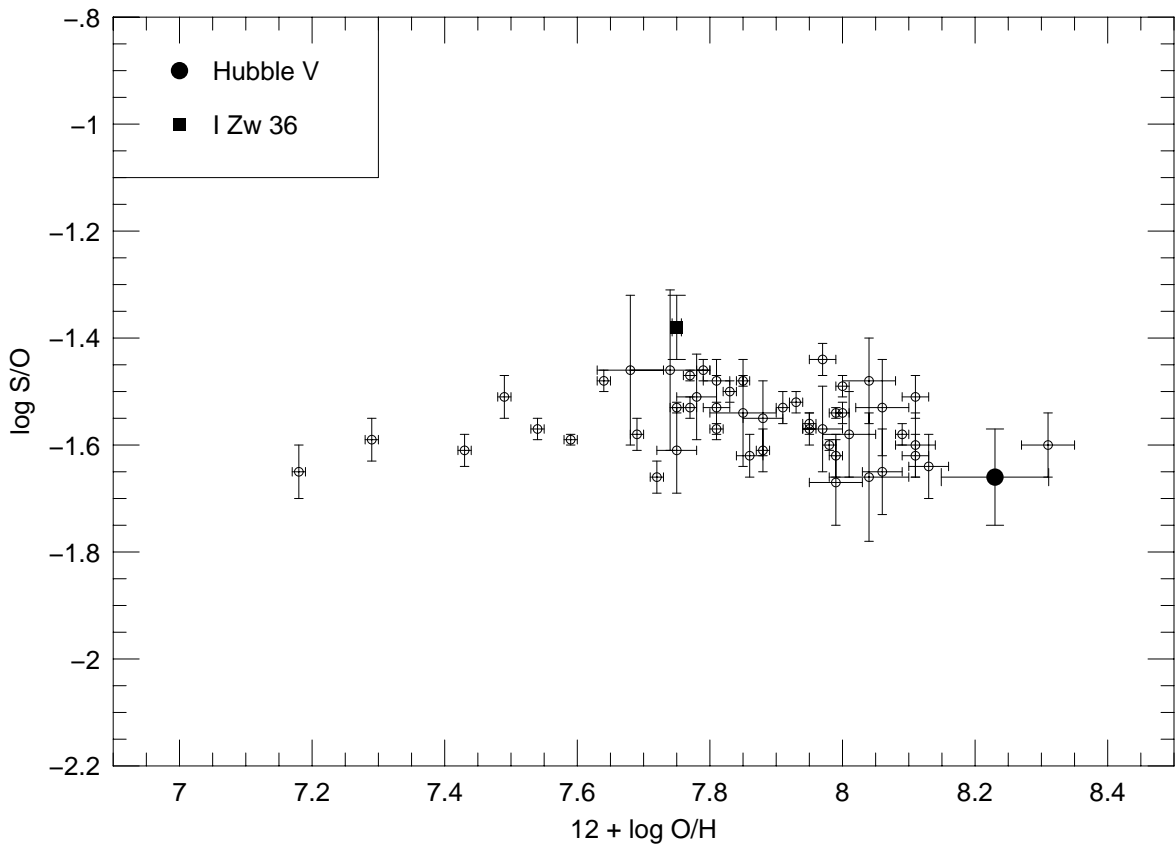


Fig. 2.— The logarithm of the ratio of S/O plotted against the logarithm of the ratio of O/H for Hubble V and I Zw 36 compared to other metal-poor HII regions from Izotov & Thuan (1999). The S/O values for Hubble V and I Zw 36 include measurements of the  $S^{+3}$  abundance from our IR observations, while the other data points rely on ionization correction factors calculated from photoionization modeling.

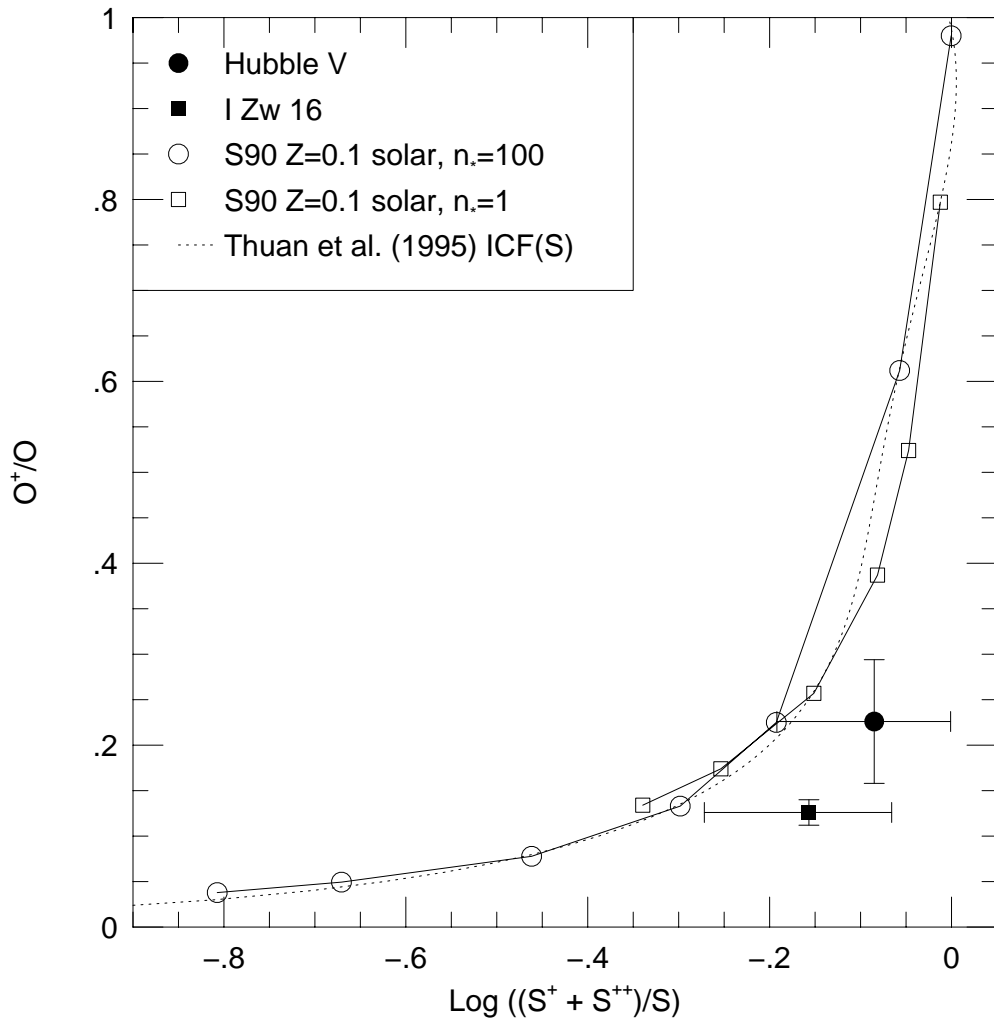


Fig. 3.—  $O^+/O$  vs.  $\text{Log } ((S^+ + S^{++})/S)$  for Hubble V and I Zw 36 compared to model nebulae using different types of model stellar atmospheres. The filled circle and square with error bars represent Hubble V and I Zw 36, respectively. Two model sequences from Stasińska (1990) having abundances of 0.1 solar and a different number of exciting stars (resulting in different ionization parameters). The stellar effective temperatures range from 32,500 K to 55,000 K. The fit to the models of Stasińska (1990) used by Thuan, Izotov & Lipovský (1995) for the sulfur ionization correction factor is given by the dotted line.

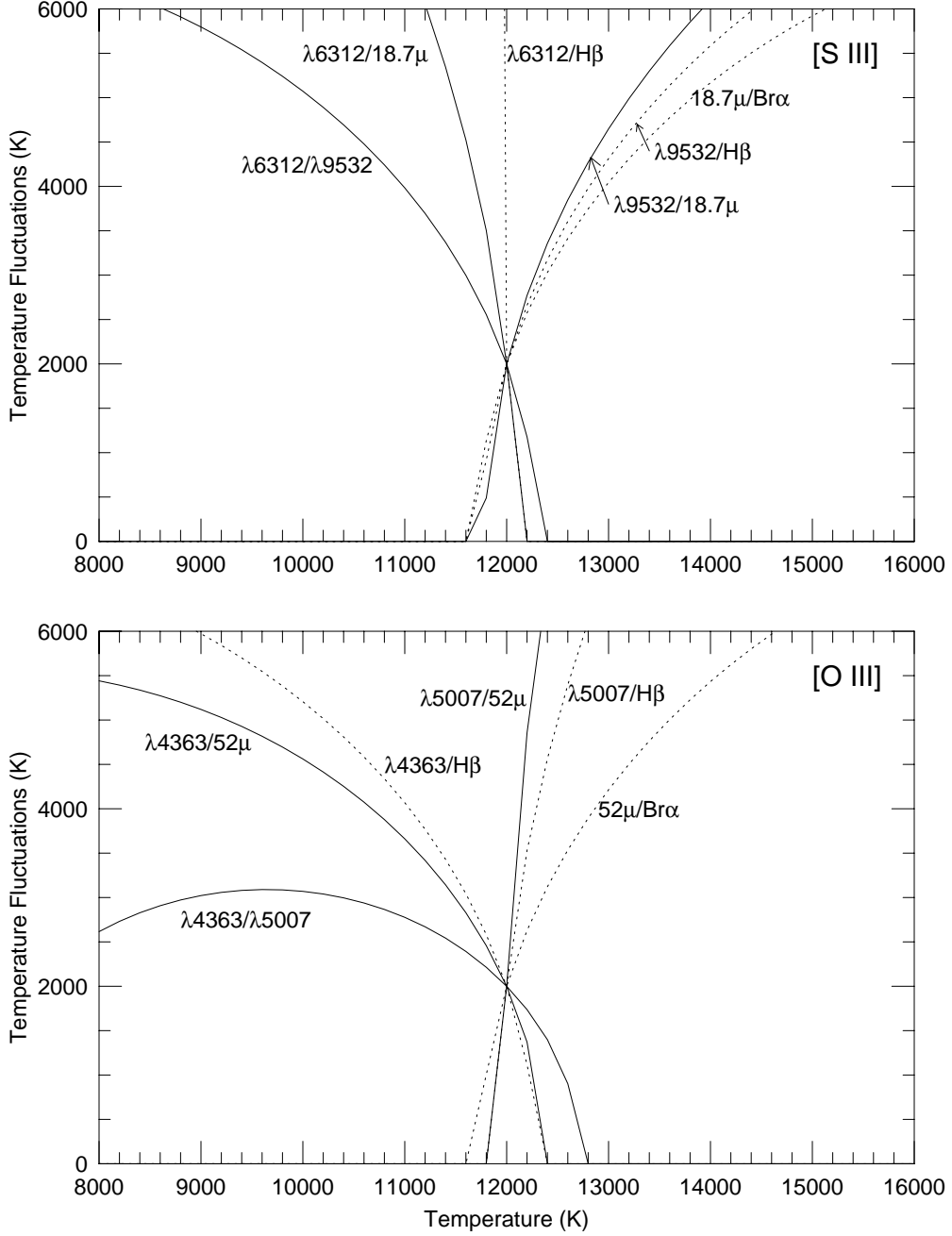


Fig. 4.— Temperature Fluctuations,  $\sigma_T$ , for a Model Nebula with input values of  $T = 12,000K$  and  $\sigma_T = 2,000K$ . *Top:* Modelled diagnostic curves using  $N(S^{+2})/N(H) = 2.92 \cdot 10^{-6}$ . *Bottom:* The corresponding graph showing diagnostic curves derived from [O III] lines.

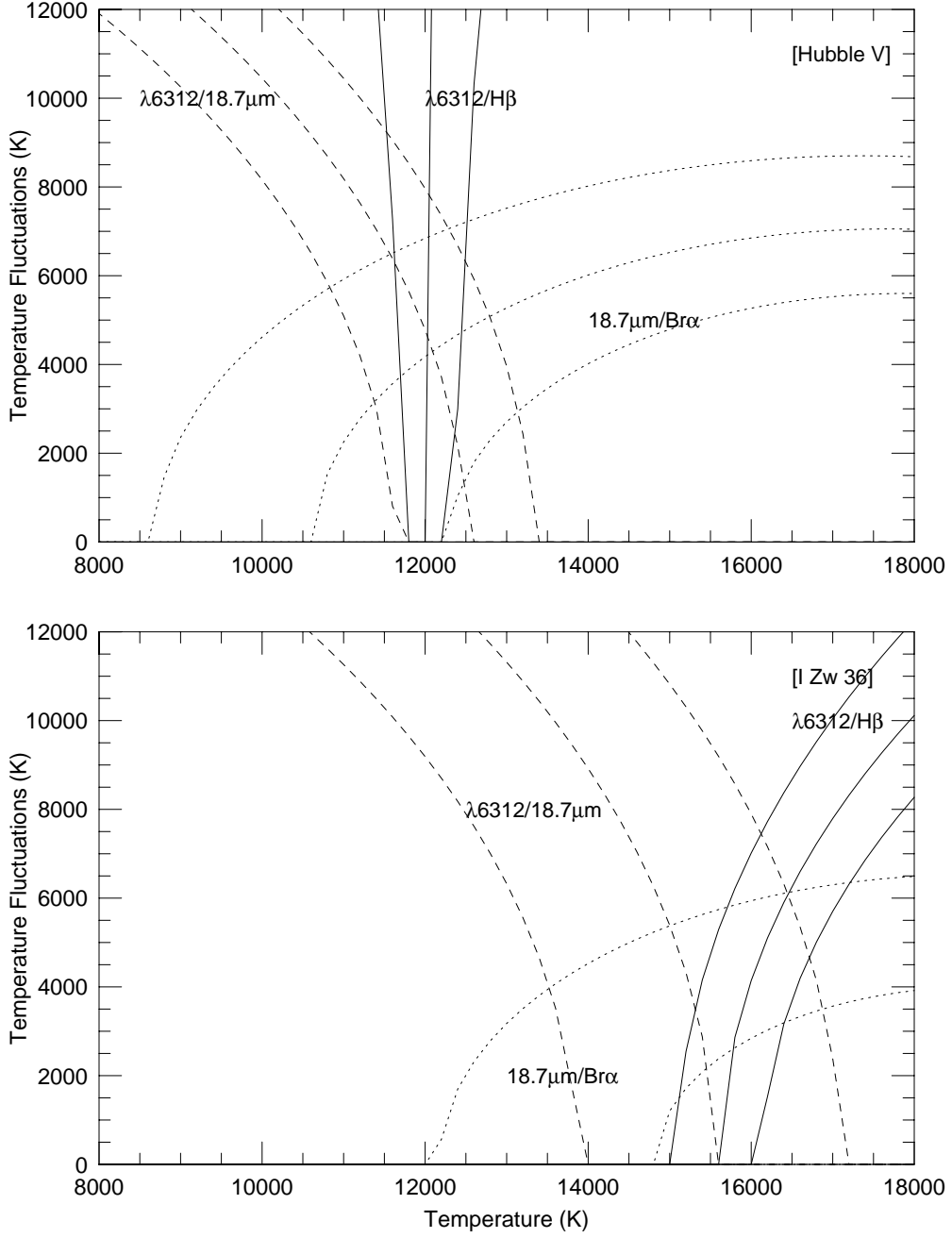


Fig. 5.— *Top:* A sample (see section 4.4.1) diagnostic for Hubble V using line strengths from this paper as well as Lequeux (1979). Groups of three roughly parallel lines are apparent. The center line of each group is the diagnostic given by the observed line ratios. The other two lines correspond to the diagnostics given by the observed line ratios  $\pm 1\sigma$ . The dashed, solid, and dotted lines correspond to the diagnostic functions from  $\lambda 6312/18.7\mu m$ ,  $\lambda 6312/H\beta$ , and  $18.7\mu m/Br\alpha$ , respectively. *Bottom:* A similar diagnostic plot for I Zw 36 using Viallefond & Thuan (1983).

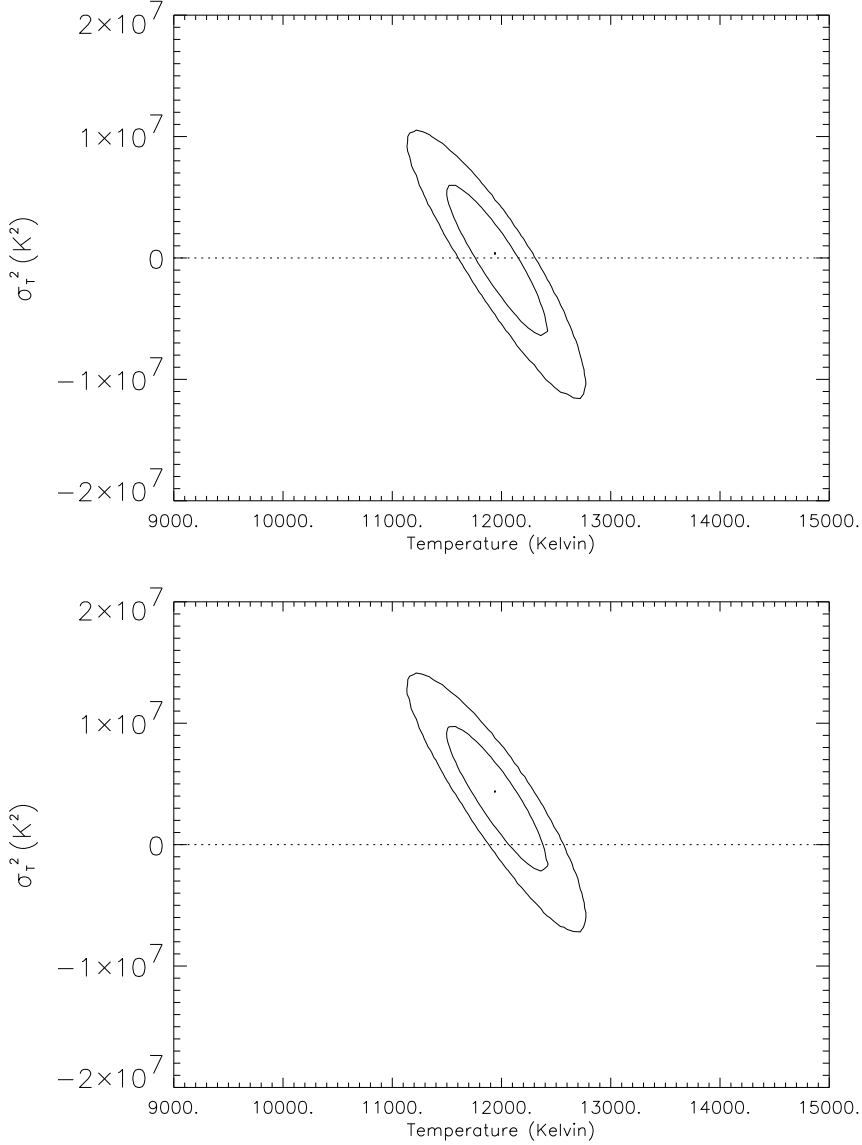


Fig. 6.— Monte Carlo Simulations showing values of  $\sigma_T^2$  vs.  $T$  derived from  $2 \cdot 10^6$  simulated observations, smeared by observational errors, based on two different cases. Contours represent 1, and  $2\sigma$  confidence levels, while the peaks of the distributions can be seen as dots in the center of the contours. In each case observational errors of 2% in the line ratios [S III]  $\lambda 6312/\lambda 9532$  and 5% in  $\lambda 9532/18.7\mu m$  were assumed. *Top:* Simulation with a specified nebular temperature of  $T = 12,000K$  with no temperature fluctuations. *Bottom:* Simulation with specified values of  $T = 12,000K$  and  $\sigma_T = 2,000K$ , corresponding to  $\sigma_T^2 = 4 \cdot 10^6 K^2$ .